Fine-scale seismic structure of the shallow volcanic crust on the East Pacific Rise at 9°50′N

Robert A. Sohn
Woods Hole Oceanographic Institution, Woods Hole, Massachusetts, USA

Spahr C. Webb
Lamont-Doherty Earth Observatory, Palisades, New York, USA

John A. Hildebrand
Scripps Institution of Oceanography, University of California, San Diego, La Jolla, California, USA

Received 23 April 2004; revised 7 September 2004; accepted 20 September 2004; published 9 December 2004.

[1] We use a combination of body wave and interface wave observations from an on-bottom seismic refraction survey to constrain the fine-scale seismic structure of the upper crust in a ~3 × 3 km field area centered on the East Pacific Rise at 9°50′N. We detonated 18 explosive shots (18 sources) in a circular pattern (1.5 km radius) on the rise axis and recorded seismic arrivals with eight ocean bottom seismometers (eight receivers). We observed 30–40 Hz compressional body waves from all shots (144 *P* waves) and 1–3 Hz Stoneley (interface) waves on a subset of source-receiver pairs (58 interface waves). Using a station correction inversion, we find that roughly half of the variance in the *P* wave first-arrival times results from lateral variations in the thickness of the surface low-velocity layer (SLVL), a layer of extremely porous lava and basalt breccia with an average *P* wave velocity of 2.2 km s^{-1}. The SLVL thickness increases from <20 m along the axial summit trough (AST) to ~120 m at near-axis lava depocenters, which are not symmetric about the rise axis. Depocenters are located ~0.5 km to the west and ~1.5 km to the east of the rise axis. Tomographic inversion of the Stoneley wave first arrivals reveals that shear velocities in the SLVL covary with the layer thickness, exhibiting a similar asymmetric pattern, with shear velocities increasing from ~320 m s^{-1} near the AST to ~520 m s^{-1} at the near-axis depocenters. Our analysis demonstrates that the seismic characteristics of the extrusive layer near the rise axis are related primarily to volcanic features and processes. The thickness and velocity of the SLVL are low on the axis and within channel networks that deliver lava flows away from the axis and then increase rapidly at the distal ends of the channels where the lavas are deposited. We find that azimuthal anisotropy exerts only a weak influence on our *P* wave first-arrival times, which we model as weak (4%) seismic azimuthal anisotropy in the upper dikes with a fast axis oriented N23°–32°W. We find no evidence for seismic azimuthal anisotropy in the extrusive layer. *INDEX TERMS:* 3025 Marine Geology and Geophysics: Marine seismics (0935); 3035 Marine Geology and Geophysics: Midocean ridge processes; 7220 Seismology: Oceanic crust; *KEYWORDS:* volcanic, seismic, structure

Citation: Sohn, R. A., S. C. Webb, and J. A. Hildebrand (2004), Fine-scale seismic structure of the shallow volcanic crust on the East Pacific Rise at 9°50′N, *J. Geophys. Res.*, *109*, B12104, doi:10.1029/2004JB003152.

1. Introduction

[2] Magmatic processes at oceanic spreading centers emplace a thin layer of lava (extrusives) at the very top of the crustal section. These high-porosity lavas provide a record of volcanic activity that can be used to study the space-time patterns of eruptions at mid-ocean ridges (MORs) [e.g., *Christeson et al.*, 1994a, 1996; *Harding et al.*, 1993; *Hooft et al.*, 1996; *Kent et al.*, 1994], and they are also an important physical and chemical interface for hydrothermal convection [e.g., *Alt*, 1995; *Sleep*, 1991]. Seismic methods play a key role in extrusive layer studies, as they can provide estimates of the layer thickness and a means to investigate structural variations related to volcanism, hydrothermal activity, and fracturing. While ship-based (i.e., sea surface) multichannel seismics are perhaps the most common method for measuring the extrusive layer thickness, fine-scale structural variations within the extrusives are best imaged with on-bottom seismic surveys that

0148-0227/04/2004JB003152$09.00

provide high-fidelity measurements of internal refractions and reflections. A fully on-bottom experiment configuration is necessitated by the geometry of seismic propagation in the shallow crust and overlying water column. The extrusive layer is much thinner than the overlying water column (typically 1/20th), and in young oceanic crust the *P* wave propagation velocities are only slightly greater (less than a factor of 2) than those in water. As a result, refractions from the extrusive layer are obscured by the high-amplitude direct water wave in most seismic records acquired using near-surface seismic sources [e.g., *Raitt*, 1963].

[3] High-fidelity measurements of extrusive layer refractions become possible when seismic sources (and receivers) are placed directly on the seafloor. While the technical aspects and logistics of placing repeatable seismic sources on the deep seafloor are formidable, this technique arguably provides the best means to image the seismic structure of the upper few hundred meters of oceanic crust. Body wave refractions from on-bottom source-receiver pairs with slant range offsets of less than ~500 m in young oceanic crust refract internally within the upper few hundred meters of oceanic crust and provide a robust means to estimate seismic velocities just beneath the seafloor-ocean interface.

[4] In this paper we present results from an on-bottom seismic refraction experiment on the East Pacific Rise (EPR) at 9°50′N designed to study the fine-scale seismic structure underlying the high-temperature vent fields found along the rise axis in this area. Our study is similar to the Near Ocean Bottom Explosives Launcher (NOBEL) East Pacific Rise Refraction Observations (NERO) experiment conducted by G. M. Purdy and G. J. Fryer on the EPR axis at 9°30′N (~36 km south of our study area) [*Christeson et al.*, 1994a] in that we use on-bottom refraction methods to resolve fine-scale variations in the seismic structure of young crust emplaced on the axis of the fast-spreading EPR. The primary differences, apart from locale, are: (1) We arranged our sources and receivers in a 3-dimensional (3-D) pattern as opposed to discrete lines for 2-D imaging; (2) we employed four-component (three geophone channels plus one hydrophone) ocean bottom seismometers (OBSs) as opposed to single-channel ocean bottom hydrophones (OBHs); and (3) we detonated our sources directly on the seafloor as opposed to within the water column. The latter two considerations proved to be especially important. By placing our sources directly on the seafloor and by measuring horizontal particle motion, we were able to generate and observe very slowly propagating Stoneley waves (waves that propagate at the interface of two homogeneous half spaces, often observed at solid-liquid interfaces) at the seafloor interface that provide excellent constraints on the *S* velocity structure of the shallow crust. These are the first observations of Stoneley waves in seismic layer 2, and they allow us to resolve lateral variations within the *S* velocity structure of mid-ocean ridge lavas for the first time, a key development since *S* velocity is highly sensitive to key rock mechanical properties such as porosity and shear modulus.

2. Experiment and Observations

[5] We deployed nine four-channel (three geophones plus one hydrophone) ocean bottom seismometers (OBSs) in a small-aperture network on the rise axis of the EPR at 9°50′N during the Temporal Observations of Eruption Seismicity (TOES) experiment from March to June 1995 (Figure 1). This portion of the rise crest was volcanically active in 1991/1992 [*Haymon et al.*, 1993; *Rubin et al.*, 1994] and is the site of several well-studied high-temperature hydrothermal vent fields [e.g., *Fornari et al.*, 1998b; *Von Damm et al.*, 1995]. The principal objective behind the OBS deployment was to study microearthquake activity beneath the high-temperature vent fields, and those aspects of the experiment are reported by *Sohn et al.* [1998, 1999].

[6] We supplemented the microearthquake survey by conducting an on-bottom seismic refraction survey. Eighteen explosive shots were detonated in a radial pattern within and around the OBS network (Figure 1). Each shot comprised 4 kg of high-density pentolite, three detraprime boosters, and a Dupont E119 blasting cap to initiate detonation. The shots were lowered to the seafloor on a wire from the R/V *New Horizon* and were detonated via an electronic trigger from a GPS clock. Returns from a 12 kHz pinger, located 50 m above the explosive package, were used to ensure that each shot was detonated directly on the seafloor rather than in the water column. The seafloor positions of the explosive shots and OBSs and the detonation times of the shots were estimated with a joint inversion [*Creager and Dorman*, 1982] using arrival times of direct and surface-reflected water waves (generated by the shots, recorded by the OBSs). The OBS positions were additionally constrained by acoustic returns from a shipboard transponder survey. The delay between the programmed versus actual detonation time for each shot was typically 120–130 ms.

[7] Seismic arrivals from the explosive shots were recorded by broadband seismometers with a flat acceleration response from 0.016 to 40 Hz and were digitized at rates of 128 Hz (vertical geophone channel and hydrophone) and 64 Hz (horizontal geophone channels). Record sections from the survey contain solid Earth phases and a series of water column multiples (Figure 2). The first solid Earth phase is a direct *P* wave (30–40 Hz) that refracts within the surface low-velocity layer (SLVL) and upper dikes. Direct crustal *P* waves were observed for all (144) source-receiver pairs. The crustal *P* wave is followed by the direct water wave, and in some cases SLVL multiples are observed between the direct crustal and water column *P* waves (Figure 2a). The water column *P* wave is followed by slowly propagating shear crustal body waves and an interface (Stoneley or Scholte) wave (Figure 2b). The crustal *S* wave can be difficult to discern in the records because it often arrives in the direct water phase wave train and has a relatively low signal level. The Stoneley waves, which were observed on ~40% (58) of the source-receiver pairs, have frequencies of ~3 Hz and are associated primarily with *S* waves turning at shallow depths in the extrusive layer. Stoneley waves have previously been observed in marine sediments [e.g., *Davies*, 1965; *Jensen and Schmidt*, 1986; *Schreiner et al.*, 1991; *Whitmarsh and Lilwall*, 1982], but this is the first time, to our knowledge, that they have been observed in seafloor lavas. In this paper we present analysis and inversions of first arrivals for the crustal *P* wave and the Stoneley wave observations.

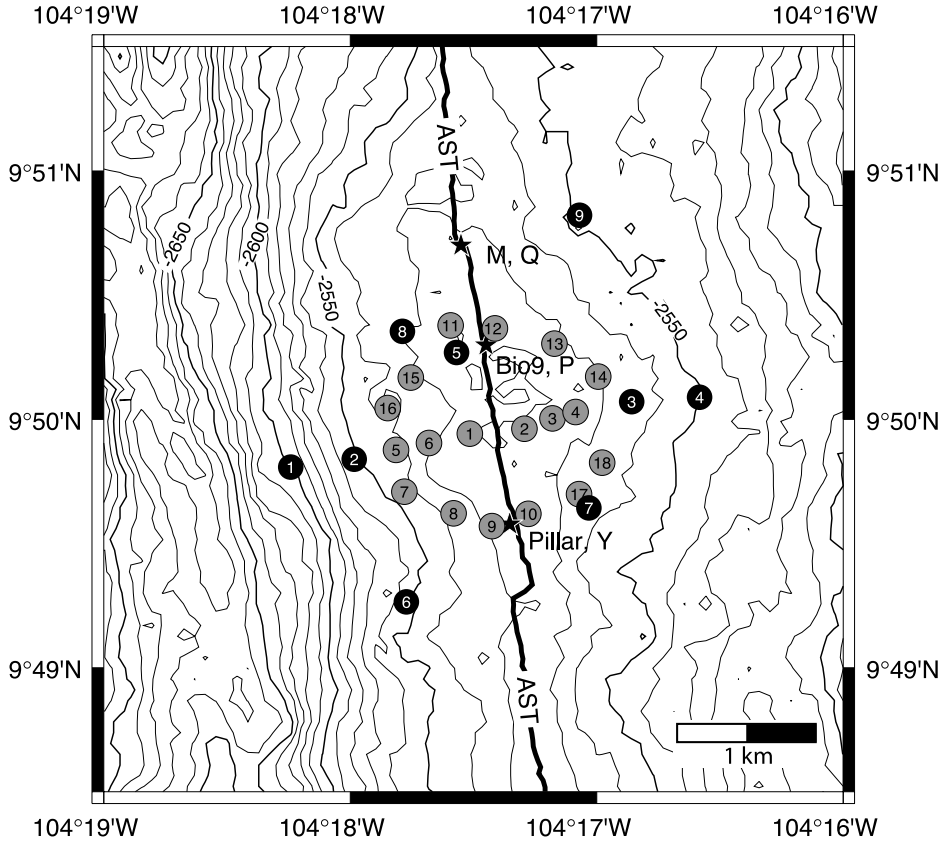

Figure 1. Experiment configuration and study area bathymetry (contours in meters). Seismic sources are shown with gray circles. Seismic receivers (OBSs) are shown with black circles. Locations of three vent fields known to be active during the experiment are shown with stars. Centerline of axial summit trough (AST) from DSL-120 side-scan imagery (D. Fornari et al., The axial summit trough of the East Pacific Rise 9°09′–59′N: New insights from DSL-120 sidescan and ABE sonar surveys, manuscript in preparation, 2004, hereinafter referred to as Fornari et al., manuscript in preparation, 2004) is shown with the heavy black line.

Analysis of *S* wave refractions and synthetic fitting of the Stoneley waveforms will be reported in a subsequent paper.

3. *P* Wave First-Arrival Data, Models, and Inversions

3.1. Average Velocity Model

[8] First-arrival travel time picks for the direct crustal *P* waves and Stoneley waves are shown in Figure 3a. Pick uncertainties are ~10 ms for the *P* waves and ~15–50 ms for the Stoneley waves. We fit the *P* wave first-arrival data with a simple, 1-D model consisting of a 100 m thick surface layer with a nearly constant V_p of 2.2 km s^{-1}, a 55 m thick high-gradient layer (47 s^{-1}), and a bottom layer with an average V_p of 4.9 km s^{-1} that extends from a depth of 155 m to the limit of ray coverage at ~ 400 m (Figure 3b). We adopt the nomenclature of *Christeson et al.* [1994a] and refer to the top layer in our model as the SLVL to distinguish it from layer 2A, which also includes the underlying high-gradient layer. Thus the SLVL in our 1-D "average" model is 100 m thick, while layer 2A is 155 m thick.

[9] Previous studies have shown that the thickness of seismic layer 2A doubles within 1–2 km of the rise axis, so we developed a more complicated starting velocity model by parameterizing the results of *Christeson et al.* [1994a]. The off-axis thickness of layer 2A in this model increases by both a thickening of the SLVL and a thickening (weakening) of the underlying gradient. We generated a 2.5-D velocity model for the study area incorporating these effects, assuming that the structural variations are symmetric about the rise axis (i.e., lateral variations in the across-axis direction only), and by "hanging" the velocity model from the local bathymetry. We used forward modeling (geometric ray tracing) to "tune" (i.e., perturb layer thicknesses and velocities) the *Christeson et al.* [1994a] results to our data and ultimately arrived at a model with residuals that have essentially the same variance as residuals from our simple, two-layer model, even though the seismic structure and ray paths in the two models are significantly different (Figure 4).

[10] The similarity of the residual variance for these two models illustrates the intrinsic nonuniqueness of velocity models based solely on arrival time data and provides some insight into modeling issues for this kind of analysis. The experiment geometry limits resolution in that ray coverage is not uniform beneath the study area, which allows for some trade-offs between SLVL thickness and the velocity of

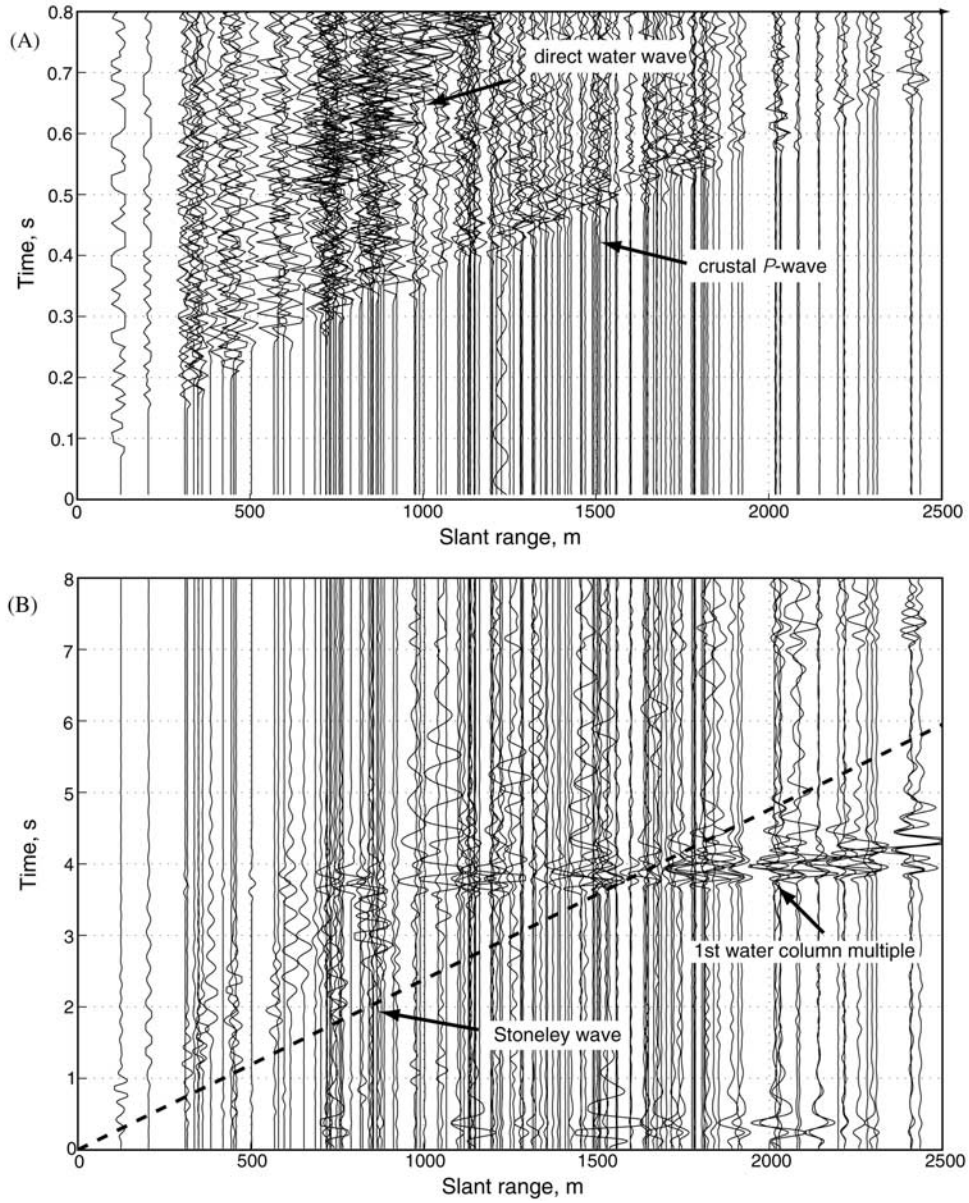

Figure 2. Pseudorecord sections (i.e., record section compiled from complete data set, not a section along a line) plotted so as to emphasize first arrivals used in analysis. (a) Raw vertical geophone components, with *P* body wave and direct water wave. (b) Horizontal component band pass filtered from 2 to 5 Hz. Dashed line represents Stoneley wave average first-arrival velocity of 420 m s^{-1}. Stoneley waves and first water column multiple are shown.

the underlying layer across the rise axis, but perhaps the most important issues pertain to heterogeneity length scale and structural asymmetry. As we will show, the shallow seismic structure is not symmetric about the rise axis in our study area, which limits the variance reduction that can be achieved by our symmetric models. We also find that there is significant structural heterogeneity in our study area with length scales that are too small to be resolved with our observations, which limits the variance reduction that can be achieved by any constrainable model. That both of our starting models achieve roughly the same variance reduction is essentially a random result that arises from the fact that neither model includes short-wavelength heterogeneities that produce much of the arrival time variance nor the structural asymmetry about the rise axis that exerts a large influence on arrival times.

[11] We lack the sort of 2-D lines that could potentially be used to formally discriminate between the two starting models, but these types of lines were in fact the basis for the results of *Christeson et al.* [1994a] that we used to parameterize the variable 2A model. This suggests that the variable 2A model may provide better insight into the volcanic lithology near the rise axis, but rather than choose between the starting models, we conducted all of our *P* wave analyses for both models in parallel. This allows us to assess the sensitivity of our results to our choice of starting model and provides perspective regarding the uniqueness of our modeling and inversions. As we will show, our primary

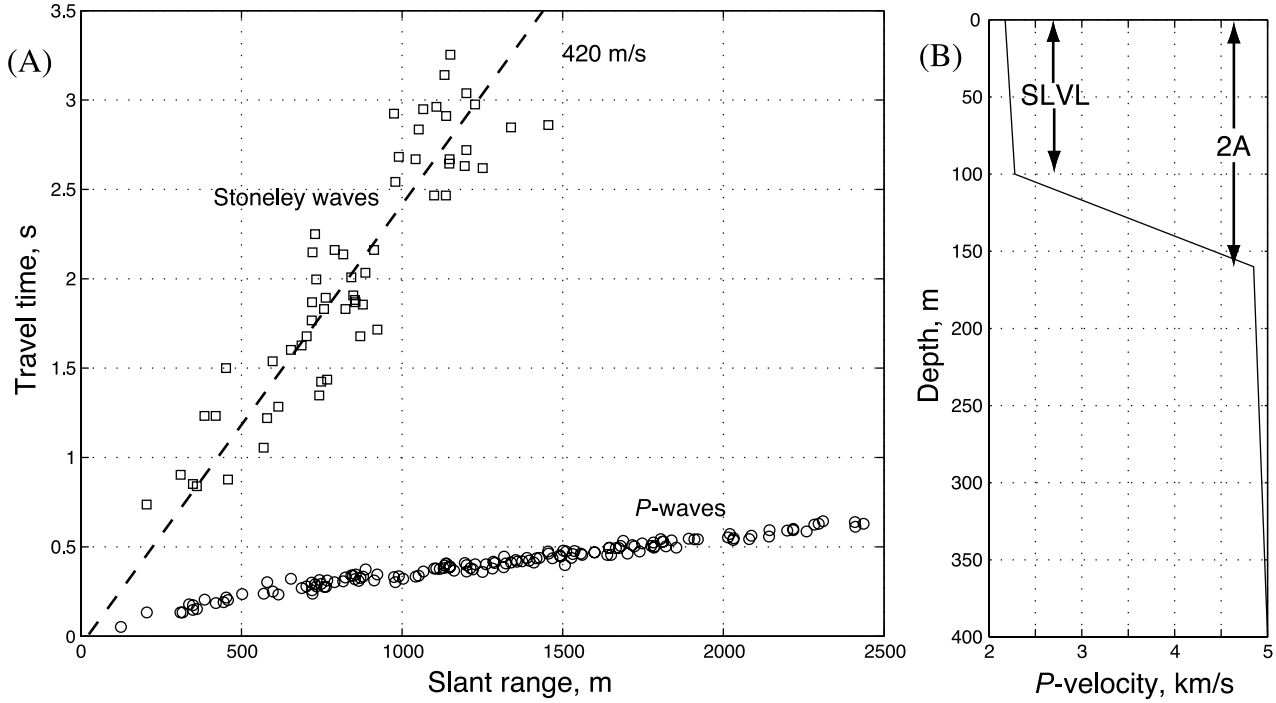

Figure 3. (a) First-arrival travel time picks for *P* waves (open circles) and Stoneley waves (open squares), with average Stoneley wave first-arrival propagation time of 420 m s^{-1} shown as a dashed line. (b) Average *P* velocity versus depth profile, with SLVL and layer 2A identified.

results are insensitive to our choice of starting model, which ultimately affects the amplitude, but not so much the nature, of the extrusive layer thickening predicted by our analysis.

3.2. Station Corrections and SLVL Thickness

[12] We used the travel time residuals between our *P* wave first-arrival observations and predictions from the 1-D average and variable 2A thickness starting models (Figures 4c and 4g) to constrain lateral variations in the seismic structure of the shallow crust. We initially attempted to parameterize inversions using lateral velocity perturbations along interfaces of constant depth, which is a standard approach for local seismic tomography, but we were unable to significantly reduce the data variance following this approach. After a great deal of trial and error we began to realize that the velocity contrast between the SLVL and the underlying layer is so strong that the critical modeling issue is to properly position this interface beneath the stations (sources and receivers), meaning that the variance in our arrival time data primarily results from thickness variations in the SLVL rather than lateral velocity variations per se.

[13] Most of the *P* wave ray paths are nearly vertical within the SLVL, which allows us to model residuals by defining a "station correction" [e.g., *Aki and Richards*, 1980, p. 610] that accounts for the travel time anomaly generated by SLVL thickness variations beneath each source and receiver. We modeled the travel time residual for each source-receiver pair as the sum of the station corrections for the source and the receiver. We then formulated an inversion to estimate the station correction for each source and receiver.

[14] We have one station correction value for each of the 18 sources and 8 receivers, yielding 26 model parameters (**m**, 26 × 1), and 144 data values representing the first-arrival residuals for each source-receiver pair with respect to the starting models (**d**, 144 × 1). The Green's matrix (also known as forward or sensitivity matrix) that expresses the relationship between the data and model has one row for each observation and one column for each model parameter (**G**, 144 × 26). Thus

$$\mathbf{d} = \mathbf{G}\mathbf{m}, \tag{1}$$

where each row of **G** has a value of 1 in the columns corresponding to the source and receiver station correction parameter for each row of **d** and zeros everywhere else. The inversion must be damped because of the low condition number of the sparse matrix **G**, which conceptually arises from the fact that the prediction error is insensitive to the addition of an arbitrarily large constant value to all station corrections. We therefore estimate the model parameters using damped least squares such that

$$\hat{\mathbf{m}} = \left[\mathbf{G}^T\mathbf{G} + \varepsilon^2\mathbf{I}\right]^{-1}\mathbf{G}^T\mathbf{d}, \tag{2}$$

where ε is the damping factor and **I** is the identity matrix.

[15] Applying this method, we obtain a station correction estimate for each source and receiver (Figure 5), yielding a variance reduction of 51% for the 1-D starting model and 47% for the variable 2A starting model, with a nominal 1σ uncertainty of 6 ms. We obtain similar station corrections (i.e., SLVL thickness perturbations) for both starting models (Table 1). The station corrections must be associated

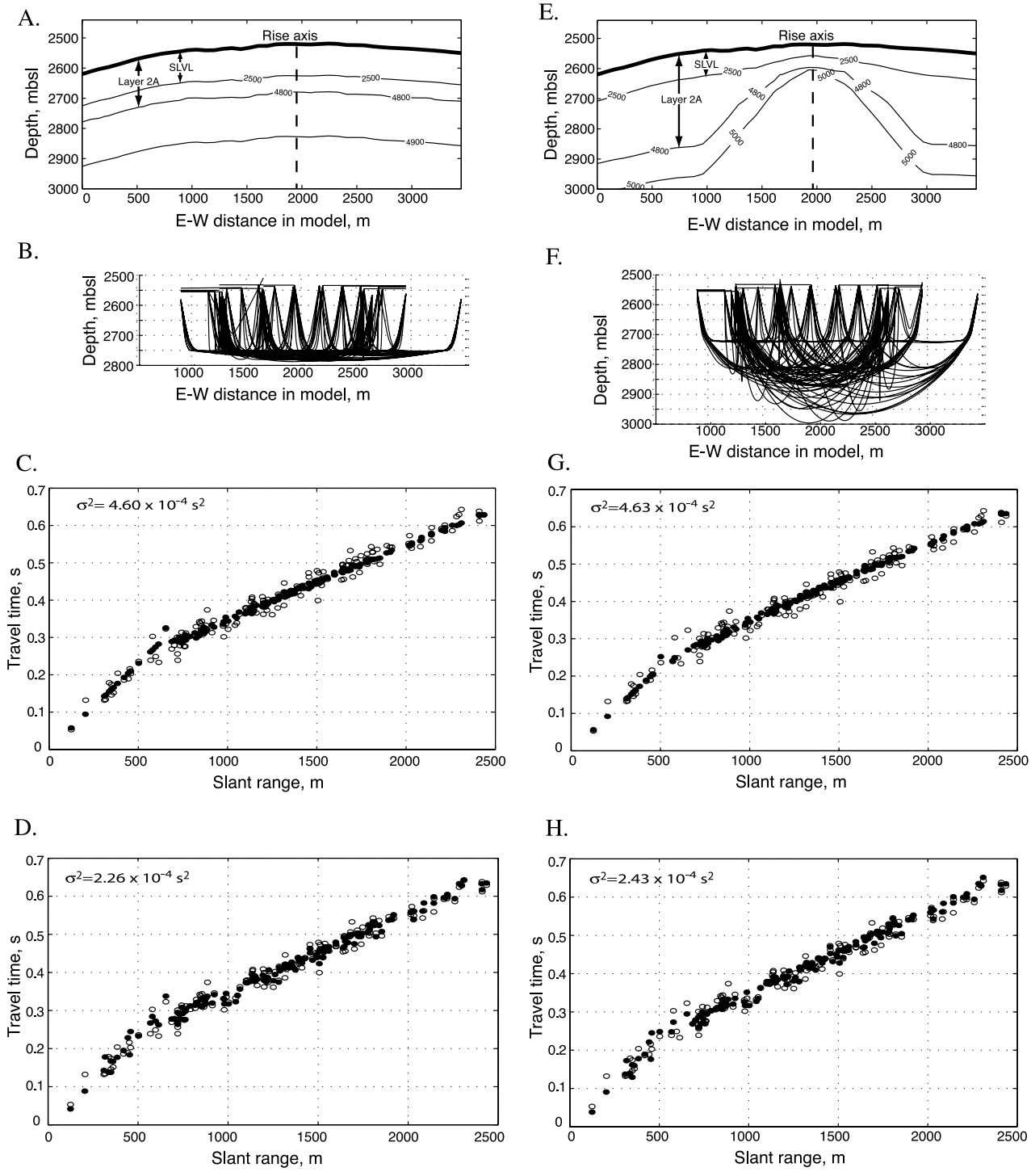

Figure 4. Starting model comparison of (a–d) one-dimensional, two-layer model and (e–h) variable 2A model. In Figures 4a and 4e, across-axis section shows model velocities as contours in m s^{-1}, with SLVL and layer 2A identified. In Figures 4b and 4f, across-axis depth section shows ray paths in the starting models. Figures 4c and 4g show fit of the travel time observations (open circles) versus model predictions (closed circles) with corresponding variance. Figures 4d and 4h show fit of the travel time observations (open circles) versus model predictions (closed circles) after application of station corrections with corresponding variance.

primarily with variations in SLVL thickness because the sign and magnitude of the values are not consistent with variations in SLVL velocity. If the station corrections resulted from lateral velocity variations, then our results would require that V_p within the SLVL decrease from a value of ~4 km s^{-1} on the rise axis to values of ~1.5 km s^{-1} at distances of ~2 km from the rise axis. This result is incompatible with a large body of research demonstrating

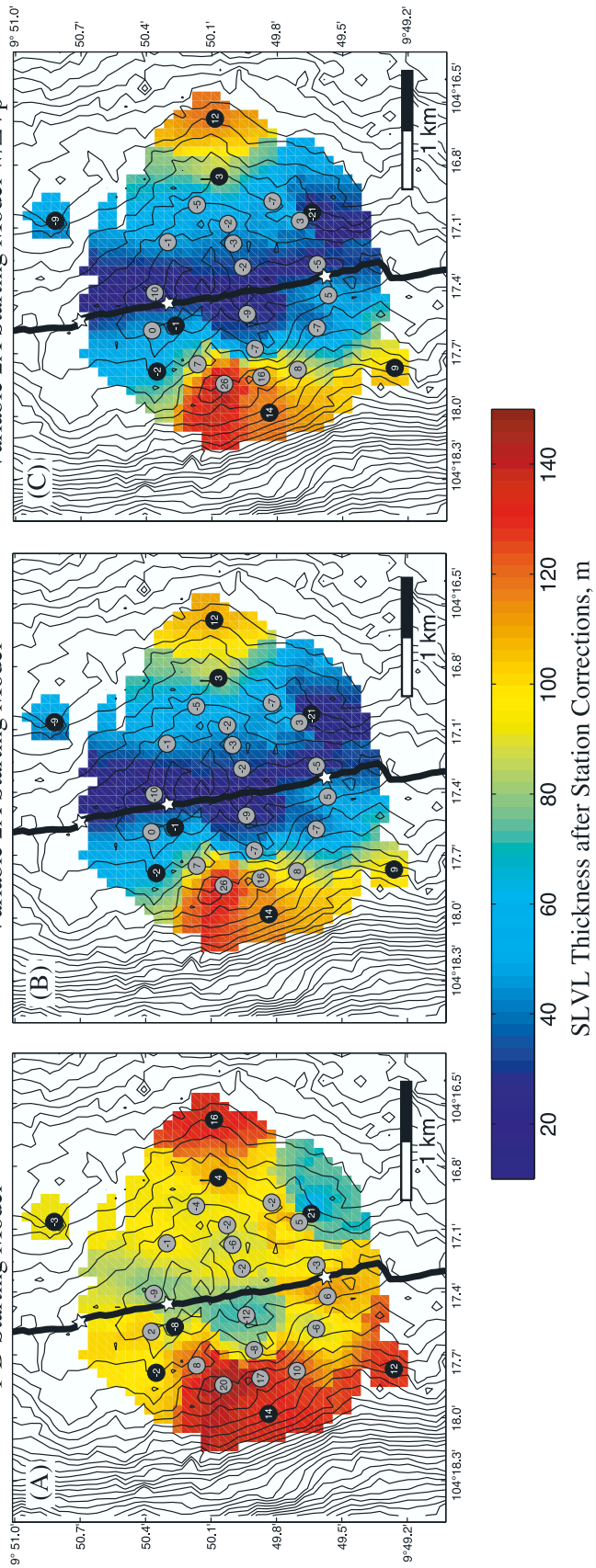

Figure 5. Station correction results and SLVL thickness for (a) the 1-D starting model, (b) the variable 2A starting model, and (c) the variable 2A starting model incorporating effects of SLVL velocity increasing away from the rise axis. Station corrections (ms) from inversion are shown as text labels inside gray circles (sources) and black circles (receivers). Final SLVL thickness estimates after application of the station corrections are plotted according to a common color map to allow for direct comparison. High-temperature vent fields known to be active in 1995 are shown as white stars. Centerline of axial summit trough (AST) from DSL-120 side-scan imagery (Fornari et al., manuscript in preparation, 2004) is shown with a heavy black line. Color contours are estimated via nearest-neighbor interpolation as described in section 5.4. Note that the color contours for Figures 5b and 5c are nearly identical, demonstrating that SLVL velocity changes away from the rise axis have a negligible effect on our layer thickness estimates.

Table 1. Station Correction Results

Station[a]	1-D Starting Model Correction, ms	Variable 2A Starting Model Correction, ms
R2	14	14
R3	4	3
R4	16	12
R5	−8	−1
R6	12	9
R7	−21	−21
R8	−2	−2
R9	−3	−9
S1	−12	−9
S2	−2	−2
S3	−6	−3
S4	−2	−2
S5	17	16
S6	−8	−7
S7	10	8
S8	−6	−7
S9	6	5
S10	−3	−5
S11	2	0
S12	−9	−10
S13	−1	−1
S14	−4	−5
S15	8	7
S16	20	26
S17	5	3
S18	−2	−7

[a]Stations are identified with source/receiver type and station ID number. For example, R2 is receiver 2, and S10 is source 10. See Figure 1 for station locations.

that the velocity of seismic layer 2A increases away from the rise axis, and it is also incompatible with our Stoneley wave analysis (section 4), which also shows that velocities in our study area increase away from the rise axis.

[16] By process of elimination we therefore associate our station corrections with SLVL thickness variations. The simplest approach for mapping station corrections into thickness variations is to assume that the average *P* wave velocity remains constant (Figures 5a and 5b). The thickness estimates, however, are relatively insensitive to the sorts of subtle velocity variations that would be expected within ~2 km of the rise axis. We included the effect of SLVL velocities increasing away from the rise axis into our mapping of station corrections into thickness estimates by incorporating our *S* velocity inverse results from section 4 and assuming that V_s/V_p is constant (Figure 5c). Thickness estimates that include lateral velocity variations are difficult to distinguish from estimates obtained assuming constant velocities (cf. Figures 5b and 5c).

[17] Our estimate of the SLVL thickness for a given site at 9°50′N depends on our choice of starting model, but the overall pattern does not. Both inversions require that the station corrections, and hence the SLVL thickness, increase moving away from the rise axis. And in both inversions we find that the thickening pattern is not symmetric about the rise axis, but rather that the SLVL thickens more rapidly on the west compared with the east side of the rise axis (Figure 6). This marked asymmetry is correlated with the local bathymetry, which falls off more rapidly to the west side of the rise axis, suggesting that the extrusive layer thickens primarily via magma effusing from the AST and then flowing downhill in channels, as we will describe in section 5.

3.3. Azimuthal Anisotropy

[18] Many studies have found evidence for seismic azimuthal anisotropy within oceanic crust on the basis of *S* wave particle motions [e.g., *Stephen*, 1981, 1985], *S* wave splitting [e.g., *Almendros et al.*, 2000; *Stephen*, 1981], and azimuthal variations in *P* velocity [e.g., *Dunn and Toomey*, 2001; *Shearer and Orcutt*, 1985; *Sohn et al.*, 1997; *White and Whitmarsh*, 1984]. Here we examine whether or not any of the remaining variance in our first-arrival data can be explained with azimuthal variations in propagation velocity. A simple plot of source-receiver azimuth versus residual amplitude (Figure 7) reveals that there is not a strong correlation between these two parameters. We used least squares methods to fit a cos (2θ) curve to these data and found that there may be a small anisotropic signal in the observations, but it is largely masked by larger amplitude variations caused by short-wavelength heterogeneities. The least squares inversion solves for the amplitude and phase of the cos (2θ) curve and the associated standard errors, yielding an amplitude of $3.6 \pm 2.45 \times 10^{-3}$ s with a fast azimuth oriented N23°W ± 19° for the 1-D model and an amplitude of $4.5 \pm 2.5 \times 10^{-3}$ s with a fast azimuth oriented N32°W ± 15° for the variable 2A model.

[19] These results are somewhat equivocal in that the amplitude parameter estimates are only slightly larger than the standard errors. However, the cos (2θ) curve fit is not a formal inversion for seismic anisotropy because it does not account for body wave polarization variations along the seismic ray paths, nor does it account for vertical variations of anisotropic parameters within the crust. Given that extrusive basalts are known to have dramatically different fracture patterns than intrusives [e.g., *van Everdingen*, 1995; *Wilkens et al.*, 1991], it seems logical to expect that the seismic anisotropy within our study area is vertically stratified. To investigate this possibility, we formulated an inversion that allows for estimation of anisotropic amplitude at four depths (0, 100, 200, and 500 m) below the seafloor [*Sohn et al.*, 1997]. The fast azimuth of anisotropy is a prior constraint that we fixed at N23°W (the result of the cos (2θ) curve fit for the 1-D starting model), and the prior variance at each node was set at $(200 \text{ m s}^{-1})^2$.

[20] The inversion was performed using residuals after station corrections for both the 1-D and variable 2A starting models. The results (Table 2) indicate that statistically significant azimuthal anisotropy is only resolved at the 200 m depth node, corresponding to the top of the dikes. A negative result is returned for the shallowest layer (0 m depth), meaning that the inverse has resolution at this depth but fails to find any evidence for anisotropy. Equivocal results are returned for the 100 and 500 m depth nodes, meaning that the inverse does not have sufficient resolution at these depths.

[21] Incorporation of weak (4–5%) azimuthal anisotropy (1-D model, 97 m s^{-1}; variable 2A model, 123 m s^{-1}, half amplitude) into our model at a depth of 200 m below the seafloor results in an additional variance reduction of 5% and 8% for the 1-D and variable 2A models, respectively. Anisotropy is therefore a subtle component of this data set,

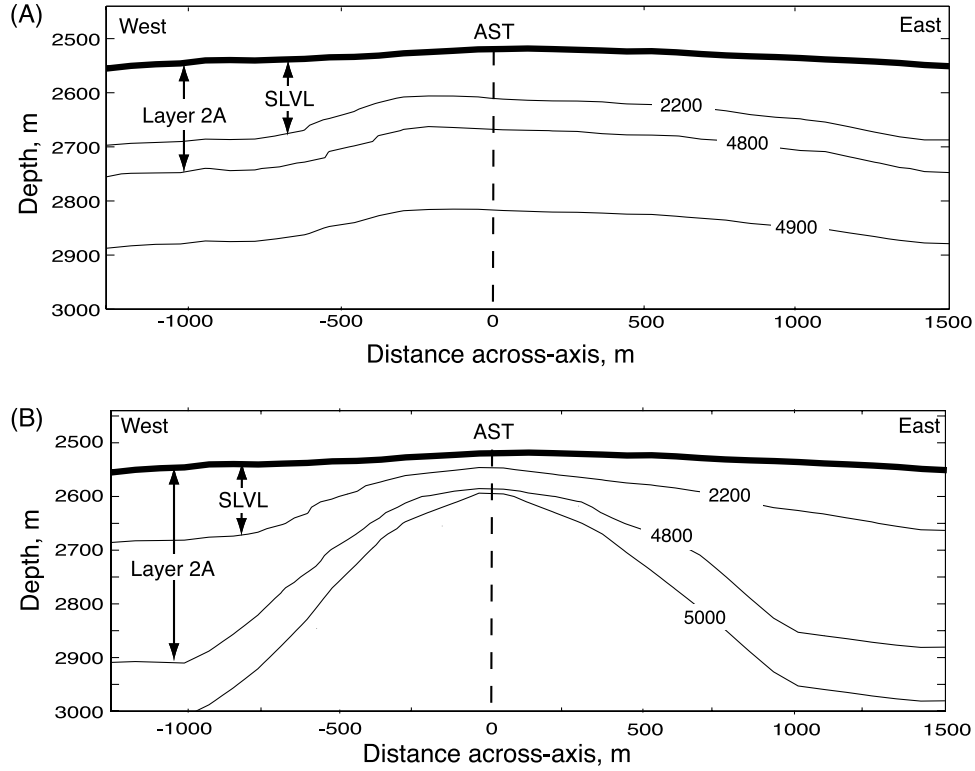

Figure 6. Seismic cross sections from the along-axis high at 9°50.0′N after station corrections for (a) the 1-D starting model and (b) the variable 2A thickness starting model. Heavy black line is seafloor topography along the cross section, with depth in m below sea surface. Contours represent P wave velocity in m s^{-1}.

and we find no evidence for anisotropy in the SLVL. The total variance reduction for the P wave first-arrival modeling (station corrections plus anisotropy) is ~56% for both models, leaving almost half of the initial variance from our starting models unaccounted for. It appears as though almost all of the variance in the P wave arrival times is acquired as the waves propagate through the SLVL. SLVL thickness variations resolvable with our station correction analysis account for about half of this variation, while the other half appears to result from unresolvable short-wavelength (<100 m) heterogeneities.

4. Stoneley Wave Data and *S* Velocity Structure

[22] We picked first arrivals for 58 Stoneley waves and used these data to formulate a tomographic inversion for lateral variations in S wave propagation speed within the SLVL within our study area. Stoneley wave first arrivals are shallow turning S body waves or S wave multiples (the Stoneley wave in a half-space model travels slightly slower than the S wave), and our inversion therefore constrains velocities in the uppermost section of the extrusive pile. Stoneley wave propagation velocities exhibit considerable variability, ranging from 275 to 590 m s^{-1} with a mean value of 420 m s^{-1} (Figure 3). These values are consistent with, though on the low side of, previous estimates of S wave velocities for young crust on the EPR based on P to S conversions at the base of layer 2A [*Christeson et al.*, 1997] and the amplitude of SLVL multiples [*Christeson et al.*, 1994a].

[23] We modeled the Stoneley wave ray paths as straight lines in a uniform half space (V_s = 420 m s^{-1}) between the source and receiver and parameterized lateral velocity variations as a truncated set of Fourier coefficients [e.g., *Sohn et al.*, 1997]. Prior spectral variances for the model parameters were weighted to impose smoothness constraints and to minimize sidelobes associated with spectral truncation. The physical size of the model domain in the inversion was increased by 50% in both the x (across-axis) and y (along-axis) directions so that the implicit periodicity of the spectral parameterization did not affect our results.

[24] The inversion seeks to minimize an objective function representing the weighted sum of the data misfit and the size of the model parameters (perturbations),

$$(\mathbf{d} - \mathbf{G}\hat{\mathbf{m}})\mathbf{C}_{dd}^{-1}(\mathbf{d} - \mathbf{G}\hat{\mathbf{m}}) + \hat{\mathbf{m}}\mathbf{C}_{mm}^{-1}\hat{\mathbf{m}} = \text{minimum}, \qquad (3)$$

where $\mathbf{d}$ is the residual of each observation with respect to an average velocity of 420 m s^{-1}, and $\mathbf{C}_{dd}$ and $\mathbf{C}_{mm}$ are the prior covariance matrices for the data and model, respectively. This equation is solved by differentiating and setting the derivative to zero, resulting in

$$\hat{\mathbf{m}} = \left(\mathbf{G}^T\mathbf{C}_{dd}^{-1}\mathbf{G} + \mathbf{C}_{mm}^{-1}\right)\mathbf{G}^T\mathbf{C}_{dd}^{-1}\mathbf{d}. \qquad (4)$$

The parameter estimates are then obtained using a damped, least squares inverse.

[25] We arrived at a final model by systematically increasing the complexity until the variance reduction tapered

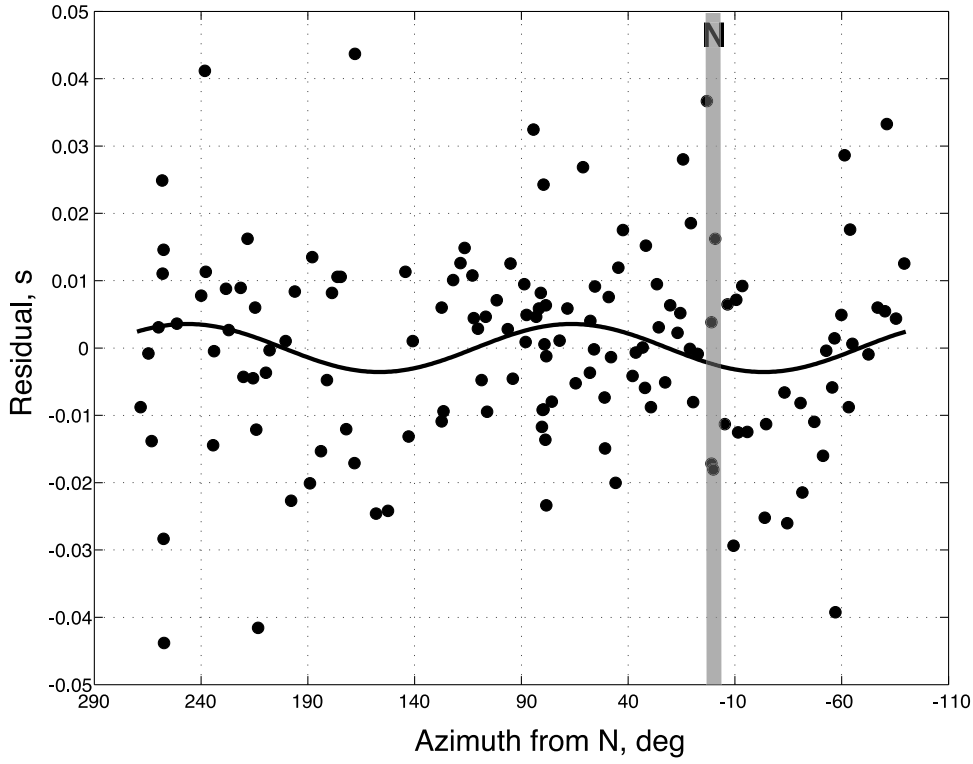

Figure 7. Travel time residuals after application of station corrections versus source-receiver azimuth. Data are shown as black circles. Cardinal direction north is shown with gray vertical band at 0°. Best fit (least squares) cos (2θ) curve is plotted as a black sinusoidal line.

off. The model complexity is determined by the number of Fourier coefficients used to parameterize the velocity perturbations in the along- and across-axis directions. We found that a systematic increase in *S* wave velocities away from the rise axis is a common feature of all the models we generated and is therefore considered to be a robust feature of the data. Our final model (Figure 8) uses three across-axis and eight along-axis Fourier coefficients and achieved a variance reduction of 74%, with formal errors as shown in Figure 8b. The nominal spatial resolution of this tomogram is 1.3 km across axis and 450 m along axis.

[26] *S* wave velocities in our model increase from minimum values of ~320 m s^{-1} near the rise axis to maximum values of ~520 m s^{-1} at distances of 1–2 km from the AST. Interestingly, the *S* velocity pattern is also asymmetric about the rise axis, similar to the SLVL thickness estimates from the station corrections, with *S* velocities increasing more rapidly to the west compared with the east of the rise axis. This covariation (Figure 9) has implications for volcanic processes near the rise axis, as we will describe below. Here we note that the sense of the arrival time residuals that generate the perturbation patterns in the SLVL thickness and *S* velocity inversions is exactly opposite. In other words, *P* wave arrivals to off-axis instruments are generally slow arrivals compared with on-axis instruments, whereas *S* wave arrivals to off-axis instruments are generally fast. This provides confidence that the covariation between SLVL thickness and *S* velocity is analytically robust and not an artifact of timing or data handling errors.

[27] Our results suggest that *S* velocities in the SLVL also vary along the ridge axis, with a decrease of ~10% moving away from the along-axis high at 9°50.1′N in either direction (Figure 8). We utilized a variety of along-axis parameterizations to investigate this apparent trend and found that

Table 2. Results From Depth-Stratified Anisotropy Inversions[a]

	1-D Model		Variable 2A Model	
Depth Below Seafloor, m	Anisotropy Amplitude, m s^{-1}	Anisotropy Uncertainty, m s^{-1}	Anisotropy Amplitude, m s^{-1}	Anisotropy Uncertainty, m s^{-1}
0	−15	98	9	125
100	−8	155	16	162
200	97	70	123	98
500	18	198	−13	157

[a]Anisotropy parameters were estimated at four depth intervals for two different isotropic seismic velocity models. Posterior uncertainties are based on prior uncertainties of 200 m s^{-1}. The inversion can best resolve anisotropy in the 200 m depth interval, where most rays turn and have nearly horizontal ray paths. The inversion also has limited resolution at 0 m where most ray paths are oriented ~30° from the vertical, but 8–10 short-range ray paths are essentially horizontal.

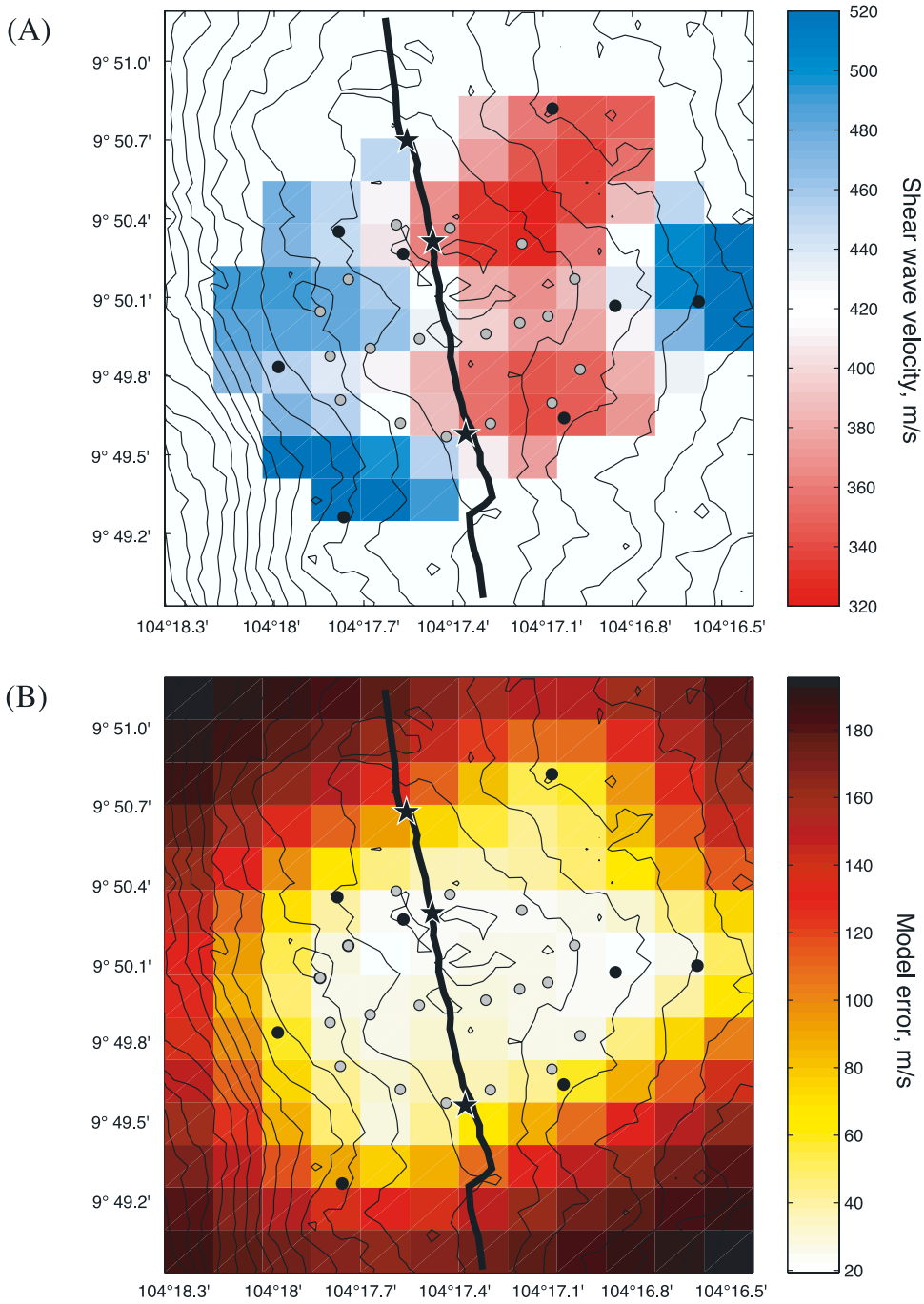

Figure 8. *S* velocity inverse results. (a) *S* velocity tomogram plotted for pixels with posterior error <100 m s^{-1}. Velocity perturbations from the inversion are added to the mean value of 420 m s^{-1} to generate absolute values of shear velocity as shown. Locations of seismic sources (gray circles), receivers (black circles), known high-temperature vent fields active in 1995 (black stars), and AST centerline (heavy black line) are shown for reference. (b) Map of posterior model error with same legend as Figure 8a.

while it is not as robust as the across-axis variations, it is a feature that appears in most of the models we produced. We discuss the possible implications of these results for volcanic and hydrothermal processes in section 5.

5. Discussion

[28] Our results are consistent with previous seismic studies of young crust on the EPR in that we find similar average seismic velocities in the shallow crust and a systematic evolution in seismic structure moving away from the rise axis [e.g., *Christeson et al.*, 1996; *Harding et al.*, 1993]. We provide new insight, however, by providing fine-scale imagery of the SLVL thickness and *S* velocity variations within a ~3 × 3 km region centered on the along-axis high at 9°50′N. The volcanic and hydrothermal features of our study area have been extremely well characterized by a relatively long history

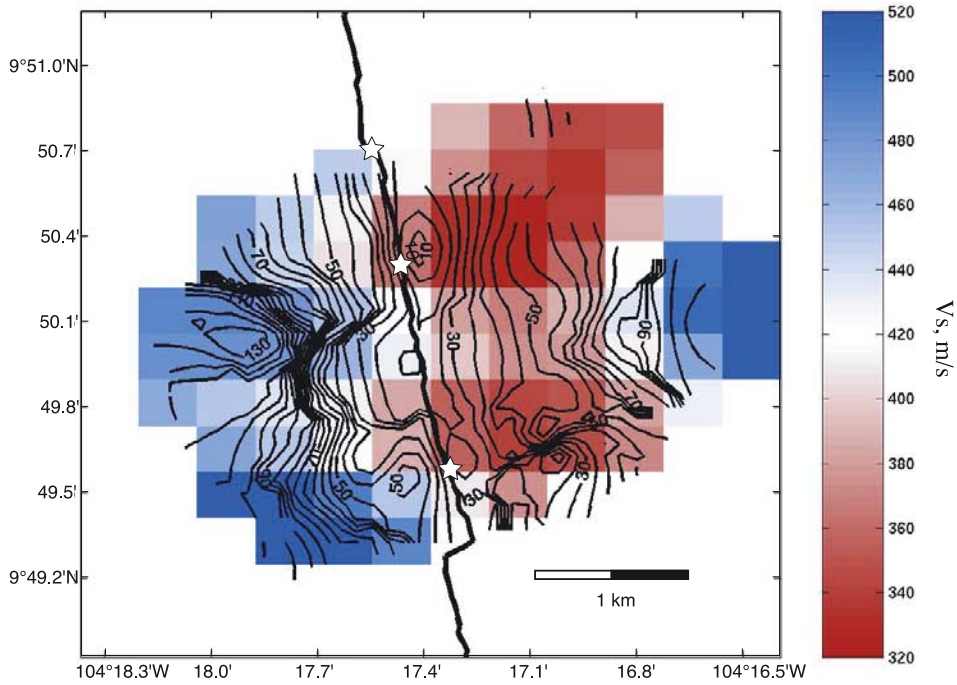

Figure 9. Covariation of SLVL thickness and *S* velocity. Thickness is shown as contours (m), and *S* velocity is shown in colors. AST centerline is shown as a heavy black line for positional reference along with three main regions of high-temperature venting (north to south equals M, Q, minus Bio9, P minus tube worm pillar, Y) shown as stars. Note how SLVL thickness contours mimic scallopy lava flow fronts in bathymetric and side-scan imagery, particularly on the west side of the AST.

of submersible observations, side-scan imagery, and near-bottom magnetic surveys [e.g., *Fornari et al.*, 2004; *Schouten et al.*, 2003; *Von Damm*, 2000], which provides excellent context for our results and allows us to carefully examine the relationship between these processes and our seismic results.

5.1. Evolution of SLVL Seismic Properties and Relationship With Volcanism

[29] The interaction between cold seawater and basaltic liquids emplaced on the seafloor during volcanic eruptions at oceanic spreading centers generates a porous and pervasively fractured lava pile with very low seismic propagation velocities. There is a strong seismic velocity contrast between the lavas and the underlying intrusives (dikes), which is particularly strong in young crust at fast-spreading centers where volcanism dominates the crustal accretion process. This contrast is immediately evident in our average *P* velocity model (Figure 3b) where a thin (~55 m) high-gradient layer separates extrusive material with *P* velocities of ~2.2 km s^{-1} from intrusive material with *P* velocities of ~4.8 km s^{-1}. Following *Christeson et al.* [1994a], we refer to the low-velocity layer at the top of our model as the SLVL, and we use the SLVL thickness as a conservative proxy for extrusive layer thickness within our study area because *P* velocities within the SLVL are too low to be associated with intrusive material. Previous studies have commonly used seismic layer 2A as a proxy for extrusive layer thickness [e.g., *Christeson et al.*, 1994a, 1996; *Harding et al.*, 1993; *Hooft et al.*, 1996; *Kent et al.*, 1994], but here we use the SLVL because, while the lithologic interpretation of the velocity gradient at the base of seismic layer 2A can be debated, there is no question that the SLVL, with *P* velocities <2.5 km s^{-1}, is composed of extrusives. Our extrusive layer thickness estimates are therefore conservative in that some fraction of the material in the underlying gradient at the base of layer 2A may be extrusive in nature, as well.

[30] The principal result of our study is the observation that the thickness and *S* velocity of the SLVL, and therefore the extrusive pile, are closely coupled and that they covary in a systematic (though asymmetric) pattern about the rise axis (Figure 9). Inspection of the local bathymetry reveals that the rise axis itself is also asymmetric (Figure 1), and all three of these data sets (SLVL thickness, SLVL *S* velocity, and bathymetry) have the same sense of asymmetry: The thickness of the extrusive pile, *S* velocities of the lava pile, and the seafloor depth all increase more rapidly to the west compared with the east of the AST. Close inspection of the microbathymetry and side-scan sonar imagery [*Fornari et al.*, 2004] reveals that the correlation between SLVL thickness and volcanic features is surprisingly specific. In the immediate vicinity of the AST the ridge has a scallopy texture representing discrete flow fronts and lava channel networks, and this texture is evident in the SLVL thickness map (Figure 10), providing compelling evidence that the

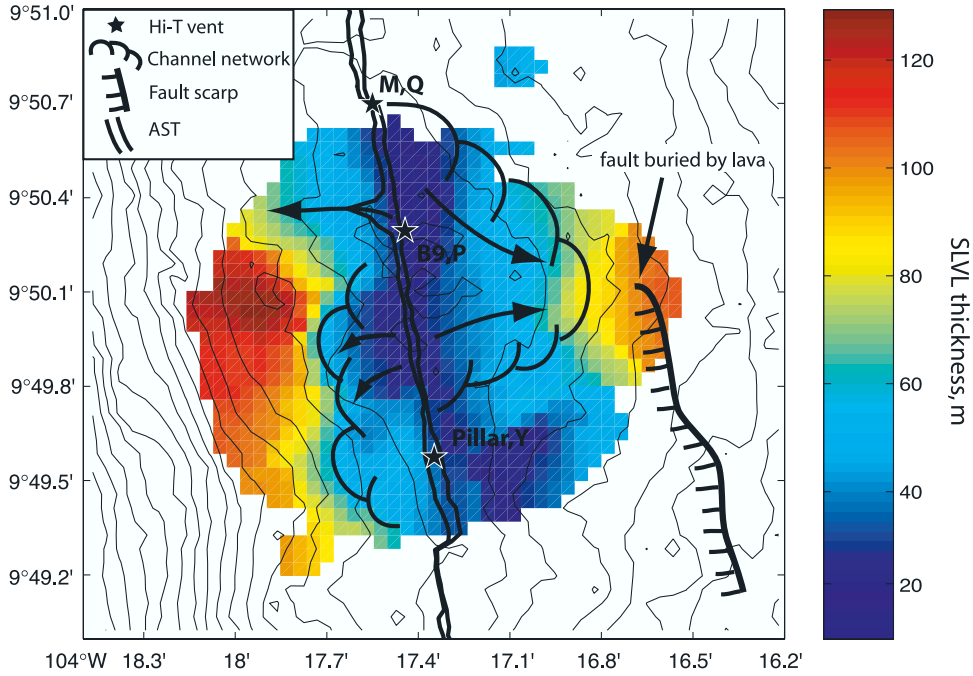

Figure 10. SLVL thickness results from the variable 2A thickness starting model (same as Figure 5b but with amplified color scale) with overlay of geological features interpreted from side-scan sonar imagery [*Fornari et al.*, 2004], submersible observations (D. Fornari and M. Tivey, personal communication, 2004), and near-bottom microbathymetry and magnetics surveys [*Schouten et al.*, 2003]. Multibeam bathymetric map with 10 m contour interval [*Cochran et al.*, 1999] is shown for reference. Eastern and western edges of AST are based on DSL-120 side-scan sonar images (Fornari et al., manuscript in preparation, 2004). Lava channel networks on the east side of the AST are confirmed with visual observations from submersible dives. Channel networks on the west side are inferred from side-scan sonar and magnetics data. Arrows indicate lateral lava flow paths inferred from the channel network geometry.

station corrections accurately render fine-scale thickness variations with the lava pile.

[31] The combination of submersible observations, microbathymetric surveys, side-scan sonar surveys, and near-bottom magnetometer surveys [*Fornari et al.*, 2004; *Schouten et al.*, 2003] has revealed the presence of lava channel networks that provide pathways for lavas to flow up to ~1.5 km away from the AST and onto the rise flanks. Some of these channels are clearly evident in microbathymetric data, but others are more difficult to image because they are shells covered with a thin roof and thus can only be unequivocally identified by visual observations. The channels terminate rather abruptly (within hundreds of meters) on the steeper west side of the AST, but on the east side the channels are longer and in at least one case appear to reach all the way to the first inward-facing fault scarp located ~1.5 km from the rise axis (Figure 10). The scarp is ~3 m high and runs roughly parallel to the rise axis but becomes buried at the edge of the lava channels, at ~9°50′8″N. Our results demonstrate that the extrusive layer thickness and *S* velocity remain low (~40 m and ~370 m s^{-1}, respectively) within this channel and then increase abruptly (>120 m and 500 m s^{-1}, respectively) at the distal end where the growth fault is buried. Minimum *S* velocities near the rise axis are as low as 320 m s^{-1}, which is somewhat lower than previous values derived from *P* to *S* conversions at the base of layer 2A (400–800 m s^{-1}) [*Christeson et al.*, 1997] and the amplitude of SLVL multiples (<750 m s^{-1}) [*Christeson et al.*, 1994a]. This small discrepancy is probably real in that the previous constraints from both the *P* to *S* conversions and SLVL multiples constrain whole layer average velocities, whereas our surface wave observations are most sensitive to *S* velocities at the very top of the SLVL, where velocities are likely to be somewhat lower than layer averages.

[32] Comparison of our results with near-bottom bathymetry geophysical imagery of the rise axis therefore reveals that the seismic characteristics of the SLVL near the rise axis are tightly coupled with volcanic features and processes. To first order we see that the thickness and *S* velocity of the extrusive layer remain low in areas where channels transport lava away from the rise axis and then increase simultaneously as the lavas pile up in near-axis depocenters. This observation lends support to the idea that eruptions primarily initiate within the AST and that lava subsequently flows downhill once the AST walls are breached [e.g., *Fornari et al.*, 1998a]. The magnitude of extrusive layer thickening deduced from our results depends on our choice of starting model for the station correction inversion. The minimum variation estimate from our 1-D starting model inversion has the SLVL thickness increasing from 60 m on the rise axis to 140 m at the near-axis depocenters. The maximum variation estimate from our variable 2A starting model has SLVL thickness increasing from <20 m

on the rise axis to 120 m at the near-axis depocenters. We are formally unable to discern between these two possibilities, but other seismic studies of layer 2A on the EPR that were configured to make measurements along 2-D flow lines and isochrons [e.g., *Christeson et al.*, 1994a, 1994b, 1996, 1997; *Hussenoeder et al.*, 2002] suggest that the results from the variable 2A starting model may be more representative of the true lithology.

[33] We cannot discern any correlation between the seismic characteristics of the SLVL and hydrothermal processes. There are three major high-temperature vent fields in our study area, and they do not appear to exert any influence on our seismic data. Thus any influence that hydrothermal processes may be exerting on the mechanical and hence seismic properties of the extrusive layer has a length scale that is too small to be observed by our experiment (<100 m). This is consistent with the fact that high-temperature vent fields on the EPR have very small seafloor expressions (tens of meters or less) and suggests that processes such as pore space infilling from interaction with cold fluids and mineral deposition are occurring at correspondingly small length scales within the lavas. This does not mean that hydrothermal alteration and mineral deposition are not an important processes for long-term "aging" and seismic evolution of layer 2A but rather suggests that these processes are not important factors in the seismic velocities of very young lavas at fast-spreading centers and/or that focused mineral deposition from high-temperature vent fields has length scales on the order of a few tens of meters.

5.2. Seismic Azimuthal Anisotropy

[34] Our analysis suggests that azimuthal anisotropy in the uppermost dike section exerts some impact on our *P* wave arrival times but that this amounts to only ~5% of the total data variance. We find evidence for weak (4–5%) azimuthal anisotropy within the uppermost dikes, which is consistent with our understanding of dike fracture patterns. Individual dikes are tabular features to first order and are emplaced as thin "blades" of magma perpendicular to the axis of least compressive stress [e.g., *Rubin*, 1992]. At mid-ocean ridges the axis of least compressive stress is generally perpendicular to the strike of the rise axis, such that dikes are emplaced in along-axis orientations. The fractures that define the margins of individual dikes are therefore preferentially aligned parallel to the rise axis [e.g., *van Everdingen*, 1995], which can generate seismic azimuthal anisotropy with a fast axis oriented along the strike of the rift zone.

[35] Our anisotropy amplitude estimate of 4–5% for the upper dikes is similar to values reported for the middle and lower dikes on the basis of *P* wave arrival time residuals from air gun refraction surveys on the EPR at 9°30′N [*Dunn and Toomey*, 2001] and the Mid-Atlantic Ridge at 35°N [*Barclay et al.*, 1998] and is slightly lower than the value of ~6% reported for the middle and lower dikes at the Juan de Fuca Ridge [*Sohn et al.*, 1997]. The air gun surveys cannot resolve anisotropy in the upper ~400 m of the crustal section for the ray geometry and propagation reasons described in section 1 [e.g., *Raitt*, 1963], and therefore our results illuminate the air gun survey results by constraining azimuthal anisotropy within their "blind spot."

[36] The fast azimuth of anisotropy in our inversions is aligned at an absolute orientation of between N23–32°W. Interestingly, this is aligned with the strike of the local rise axis as opposed to the larger-scale plate boundary, which strikes at N9°W. This suggests that the strike of the dike section, and hence the local stress field, deviates by ~14° with respect to the larger-scale plate boundary. We can only speculate regarding the possible causes of this rotation, but we note that the Lamont seamount chain intersects the EPR at 9°50′N, raising the possibility that interaction between the melting anomaly that generates the seamount chain and the spreading center has locally perturbed the stress field [e.g., *Pockalny et al.*, 1997].

[37] Our depth-stratified anisotropy inversion returns a negative result for the extrusives, arguing against seismic azimuthal anisotropy in this upper layer. If we take this result at face value, then our results suggest that the aggregate fracture set that controls seismic velocity in the extrusives is not preferentially aligned. This is consistent with extrusive velocities being controlled by thin, high aspect ratio fractures resulting from rapid thermal contraction and flow deformation, as opposed to larger scale tectonism. Larger-scale fissures, such as the AST itself, which are obviously preferentially aligned with the rise axis and penetrate into the extrusive layer, do not appear to exert a significant impact on average velocities. More work may be required, however, to verify this null result since we have but a handful of rays that refract entirely within the SLVL. Our negative anisotropy result for the extrusive layer contrasts with the study of *McDonald et al.* [1994] on the Cleft segment of the Juan de Fuca Ridge, which reported an extrusive layer anisotropy of ~19% on the basis of analysis of *P* wave residuals in air gun refraction data. Our results are probably more robust in that our on-bottom experiment configuration provides first-arrival observations at very short source-receiver offsets for phases that propagate nearly horizontally within the extrusive layer, which is ideal for constraining anisotropy, but we cannot rule out the possibility that extrusive layer anisotropy is a site-specific characteristic. More studies are clearly needed to determine the nature of vertically stratified anisotropy within layer 2 and to assess variability between geologic/tectonic environments (i.e., fast versus slow or intermediate spreading).

5.3. Elastic Characteristics of the Extrusive Layer

[38] The elastic/mechanical characteristics of the extrusive layer are important for understanding the relationship between crustal deformation and seafloor geology and for understanding how tidal loading and stress perturbations from nearby earthquakes may influence hydrothermal circulation within the shallow crust. The elastic characteristics of a solid material are uniquely determined by three parameters: V_p, V_s, and ρ (density). In this study we have constrained V_p and V_s, and the average density of the extrusive layer at 9°50′N has been previously constrained by seafloor [*Stevenson and Hildebrand*, 1996] and near-bottom [*Cochran et al.*, 1999] gravimetric measurements. As a result, we are in a unique position to estimate the elastic characteristics of the extrusive layer at this site, which are shown in Table 3.

[39] The most striking aspect of these estimates is the extremely low shear modulus of 425 MPa that arises from

Table 3. Elastic Parameters Derived for the Extrusive Layer at 9°50′N on the Basis of Average Values of V_p = 2.2 Versus 0.42 km s^{-1} and Density = 2410 kg m^{-3}

Parameter	Value
Shear modulus, $\mu = \rho\beta^2$	425 MPa
Lambda parameter, $\lambda = \alpha^2\rho - 2\mu$	10.8 GPa
Poisson's ratio, $\sigma = \lambda/[2(\lambda + \mu)]$	0.48
Bulk modulus, $\kappa = \lambda + (2\mu/3)$	11.1 GPa
Young's modulus, $E = \mu[(3\lambda + 2\mu)]/(\lambda + \mu)$	1.3 GPa

the low *S* velocities we measured from the interface waves. This indicates that the top of the extrusive layer near the rise axis is a combination of massively porous channels and essentially unconsolidated basaltic rubble. This layer has almost no shear strength, indicating that the rock behaves similar to a fluid (Poisson's ratio equals 0.48). The lateral variations in *S* velocity we have imaged translate into corresponding variations in shear modulus. Our results indicate that the shear modulus increases from a value of 247 MPa on the rise axis to a value of 602 MPa ~1.5 km from the rise axis. The shear strength of the extrusive layer therefore more than doubles over this length interval. The very low shear modulus values we obtain for the extrusive layer preclude the development of significant levels of differential stress or strain in the extrusives, and we may expect this layer to deform more like a pile of bricks rather than a coherent solid matrix. The shear modulus results also have implications for poroelastic modeling of the effects of ocean tides on hydrothermal circulation, which is sensitive to the elastic parameters of the extrusive layer [e.g., *Jupp and Schultz*, 2004; *Wang and Davis*, 1996]. Our constraints on lateral variability of elastic parameters may eventually prove useful for future modeling efforts when they begin to address 2- and 3-dimensional systems.

5.4. Inverse Resolution and Regularization

[40] We made seismic velocity models from three different data inversions: (1) station correction inversion, (2) depth-stratified azimuthal anisotropy inversion, and (3) Stoneley wave *S* velocity inversion. These inversions have disparate resolutions and regularization schemes, as we describe here. As described in section 3.2, station corrections are effectively point measurements, and there is no formal regularization scheme applied to the inversion. Ray paths beneath each source and receiver form an inverted cone within the SLVL, and the length scale of this cone represents an effective regularization since the estimates are formulated by averaging over all of the ray paths in a cone. The radius of a cone beneath a given station depends on the SLVL thickness and the propagation angle of the seismic rays therein. In this experiment the nominal propagation angle within the SLVL is ~30° for most rays (i.e., turning in the upper dikes), and if we take the SLVL as ranging from 20 to 120 m, then we find that the station corrections represent thicknesses averaged over lateral length scales of 12–70 m. For graphical purposes we produced contour maps of SLVL thickness by generating a Cartesian grid with nodes spaced every 80 m in the north-south and east-west directions and then interpolating between the two nearest stations within 600 m of the grid node. The 600 m distance threshold was determined via trial and error.

[41] The depth-stratified anisotropy inversion does not incorporate lateral variations, and the resolution is therefore limited to the vertical axis. We parameterized the vertical variations as triangle functions, which assume that the magnitude of anisotropy varies linearly between vertical nodes. The spatial resolution is controlled by the number and location of the depth interfaces chosen for parameterizing the inversion. Our choice of depth nodes was based primarily on the relationship of the ray path geometry for the two starting models with the inferred lithologic stratification (Figures 4b and 4f) and a desire to minimize the number of degrees of freedom in the inverse. Here again we used trial and error to arrive at a final parameterization. The ability of the inverse to resolve anisotropy at each discrete depth node is quantified by the diagonal elements of the posterior covariance matrix or model error (Table 2).

[42] The lateral resolution of the Stoneley wave first-arrival inversion for *S* velocity structure is a function of the number of Fourier coefficients used to parameterize variations in the along- and across-axis directions. In contrast to the station corrections, the *S* velocity models therefore do have prior smoothness constraints with explicit length scales determined by the wavelengths of the Fourier coefficients and by spectral weighting via specification of prior model variances.

[43] The net result is that our models of *S* velocity and SLVL thickness have dramatically different spatial parameterizations and smoothness constraints. Thickness estimates can vary dramatically from one nearby station to the next (e.g., OBS 7 and shot 17), whereas *S* velocities cannot, because they are regularized as described above. For example, the minimum axis of the *S* velocity model is offset a few hundred meters east of the AST (Figure 8) such that *S* velocities are higher in the AST than they are a few hundred meters to the east. This is almost certainly not the case but rather reflects the effect of regularization since the inverse is trying to model the effects of structural asymmetry about the rise axis with a finite set of Fourier coefficients.

6. Summary

[44] We use observations from an on-bottom seismic refraction survey to constrain the fine-scale seismic structure of the upper ~250 m of volcanic crust on the EPR at 9°50′N. Our principal results are that

[45] 1. The seismic structure of our study area is capped by a low-velocity layer (SLVL) with average *P* velocities of ~2.2 km s^{-1} and with *S* velocities of ~420 m s^{-1} near the top of the layer. We are able to model ~50% of the variability in *P* wave first-arrival times with respect to our starting models as SLVL thickness variations and ~74% of the Stoneley wave first-arrival times as later velocity variations.

[46] 2. SLVL thickness increases systematically off axis. In a conservative (minimum variation) model the thickness increases from 60 m on the rise axis to 140 m at a distance of ~1.5 km from the axis. In a more aggressive model that incorporates constraints from other seismic experiments, the thickness increases from <20 m on the rise axis to 120 m at 1.5 km off axis.

[47] 3. *S* velocity covaries with SLVL thickness, with minimum velocities of ~320 m s^{-1} on the rise axis increasing to ~500 m s^{-1} at 1–1.5 km away from the AST. The patterns of SLVL thickness and *S* velocity are both asymmetric about the AST and increase more rapidly on the west side of the rise axis where the bathymetric gradient is steeper.

[48] 4. The SLVL thickness estimates are correlated with seafloor volcanic features imaged by complementary near-bottom geophysical surveys and closely mimic the scallopy lava flow pattern observed in microbathymetric and side-scan sonar surveys. This supports the concept that these features are channels that provide primary pathways for lavas erupting out of the AST and then subsequently flowing downhill. The SLVL thickness is observed to increase abruptly at lava depocenters located at the distal end of the channels.

[49] 5. There is weak (4–5%) azimuthal anisotropy within the upper dikes with a fast axis oriented with the local ridge strike at N23–32°W. No evidence for azimuthal anisotropy is found in the SLVL.

[50] 6. The shear modulus of the SLVL varies from ~250 MPa in channel networks on the rise axis to ~600 MPa at the near (1.5 km) axis lava depocenters.

[51] 7. We are unable to account for ~45% of the variance in the *P* wave first-arrival data, indicating that heterogeneities with length scales less than the resolving power of our study (~100 m) exert a significant influence on seismic propagation within the upper ~250 m of crust.

[52] **Acknowledgments.** The authors thank Jacques Lemire and Tom Deaton for engineering support for the ocean bottom seismometers and John Boaz for technical support at sea. The manuscript has benefited significantly from discussions with Gail Christeson, Suzanne Carbotte, Alistair Harding, Maurice Tivey, Dan Fornari, and Hans Schouten and from thoughtful reviews by Andrew Barclay, Fred Simons, and an anonymous reviewer.

References

Aki, K., and P. G. Richards (1980), *Quantitative Seismology, Theory and Methods*, W. H. Freeman, New York.

Almendros, J., A. H. Barclay, W. S. D. Wilcock, and G. M. Purdy (2000), Seismic anisotropy on the Juan de Fuca Ridge from observations of shear-wave splitting, *Geophys. Res. Lett.*, *27*, 3109–3112.

Alt, J. C. (1995), Subseafloor processes in mid-ocean ridge hydrothermal systems, in *Seafloor Hydrothermal Systems: Physical, Chemical, Biological, and Geological Interactions*, *Geophys. Monogr. Ser.*, vol. 91, edited by S. E. Humphris et al., pp. 85–114, AGU, Washington, D. C.

Barclay, A. H., D. R. Toomey, and S. C. Solomon (1998), Seismic structure and crustal magmatism at the Mid-Atlantic Ridge, 35°N, *J. Geophys. Res.*, *103*, 17,827–17,844.

Christeson, G. L., G. M. Purdy, and G. J. Fryer (1994a), Seismic constraints on shallow crustal emplacement processes at the fast spreading East Pacific Rise, *J. Geophys. Res.*, *99*, 17,957–17,973.

Christeson, G. L., W. S. D. Wilcock, and G. M. Purdy (1994b), The shallow attenuation structure of the fast-spreading East Pacific Rise near 9°30′N, *Geophys. Res. Lett.*, *21*, 321–324.

Christeson, G. L., G. M. Kent, G. M. Purdy, and R. S. Detrick (1996), Extrusive thickness variability at the East Pacific Rise, 9°10°N: Constraints from seismic techniques, *J. Geophys. Res.*, *101*, 2859–2873.

Christeson, G. L., P. R. Shaw, and J. D. Garmany (1997), Shear and compressional wave structure of the East Pacific Rise, 9°–10°N, *J. Geophys. Res.*, *102*, 7821–7835.

Cochran, J. R., D. J. Fornari, B. J. Coakley, R. Herr, and M. A. Tivey (1999), Continuous near-bottom gravity measurements made with a BGM-3 gravimeter in DSV *Alvin* on the East Pacific Rise crest near 9°31′N and 9°50′N, *J. Geophys. Res.*, *104*, 10,841–10,861.

Creager, K. C., and L. M. Dorman (1982), Location of instruments on the seafloor by joint adjustment of instrument and ship positions, *J. Geophys. Res.*, *87*, 8379–8387.

Davies, D. (1965), Dispersed Stoneley waves on the ocean bottom, *Bull. Seismol. Soc. Am.*, *55*, 903–918.

Dunn, R. A., and D. R. Toomey (2001), Crack-induced seismic anisotropy in the oceanic crust across the East Pacific Rise (9°30′N), *Earth Planet. Sci. Lett.*, *189*, 9–17.

Fornari, D. J., R. M. Haymon, M. R. Perfit, T. K. P. Gregg, and M. H. Edwards (1998a), Axial summit trough of the East Pacific Rise 9°–10°N: Geological characteristics and evolution of the axial zone on fast spreading mid-ocean ridges, *J. Geophys. Res.*, *103*, 9827–9855.

Fornari, D. J., T. M. Shank, K. L. Von Damm, T. K. P. Gregg, M. Lilley, G. Levai, A. Bray, R. M. Haymon, M. R. Perfit, and R. A. Lutz (1998b), Time-series temperature measurements at high-temperature hydrothermal vents: East Pacific Rise 9°49′N to 9°51′N: Monitoring dike intrusion and crustal cracking events, *Earth Planet. Sci. Lett.*, *160*, 419–431.

Fornari, D., et al. (2004), Submarine lava flow emplacement at the East Pacific Rise 9°50′N: Implications for uppermost ocean crust stratigraphy and hydrothermal fluid circulation, in *Mid-Ocean Ridges: Hydrothermal Interactions Between the Lithosphere and Oceans*, *Geophys. Monogr. Ser.*, vol. 148, edited by C. R. German, J. Lin, and L. M. Parson, pp. 187–218, AGU, Washington, D. C.

Harding, A. J., G. M. Kent, and J. A. Orcutt (1993), A multichannel seismic investigation of upper crustal structure at 9°N on the East Pacific Rise: Implications for crustal accretion, *J. Geophys. Res.*, *98*, 13,925–13,944.

Haymon, R. M., et al. (1993), Volcanic eruption of the mid-ocean ridge along the East Pacific Rise crest at 9°45–52′N: Direct submersible observations of seafloor phenomena associated with an eruption event in April, 1991, *Earth Planet. Sci. Lett.*, *119*, 85–101.

Hooft, E. E. E., H. Schouten, and R. S. Detrick (1996), Constraining crustal emplacement processes from the variation in seismic layer: 2. A thickness at the East Pacific Rise, *Earth Planet. Sci. Lett.*, *142*, 289–309.

Hussenoeder, S. A., R. S. Detrick, G. M. Kent, H. Schouten, and A. J. Harding (2002), Fine-scale seismic structure of young upper crust at 17°20′S on the fast spreading East Pacific Rise, *J. Geophys. Res.*, *107*(B8), 2158, doi:10.1029/2001JB001688.

Jensen, F. B., and H. Schmidt (1986), Shear properties of ocean sediments determined from numerical modeling of Scholte wave data, in *Ocean Seismo-Acoustics: Low-Frequency Underwater Acoustics*, edited by T. Akal and J. M. Berkson, pp. 683–692, Plenum, New York.

Jupp, T. E., and A. Schultz (2004), A poroelastic model for the tidal modulation of seafloor hydrothermal systems, *J. Geophys. Res.*, *109*, B03105, doi:10.1029/2003JB002583.

Kent, G. M., A. J. Harding, J. A. Orcutt, R. S. Detrick, J. C. Mutter, and P. Buhl (1994), Uniform accretion of oceanic crust south of the Garret transform at 14°15′S on the East Pacific Rise: Implications for crustal accretion, *J. Geophys. Res.*, *99*, 9097–9116.

McDonald, M. A., S. C. Webb, J. A. Hildebrand, B. D. Cornuelle, and C. G. Fox (1994), Seismic structure and anisotropy of the Juan de Fuca Ridge at 45°N, *J. Geophys. Res.*, *99*, 4857–4873.

Pockalny, R. A., P. J. Fox, D. J. Fornari, K. C. Macdonald, and M. R. Perfit (1997), Tectonic reconstruction of the Clipperton and Siqueiros Fracture Zones: Evidence and consequences of plate motion change for the last 3 Myr, *J. Geophys. Res.*, *102*, 3167–3181.

Raitt, R. W. (1963), The crustal rocks, in *The Sea: The Earth Beneath the Sea*, edited by M. N. Hill et al., pp. 85–102, John Wiley, Hoboken, N. J.

Rubin, A. M. (1992), Dike-induced faulting and graben subsidence in volcanic rift zones, *J. Geophys. Res.*, *97*, 1839–1858.

Rubin, K. H., J. D. Macdougall, and M. R. Perfit (1994), ^{210}Po-^{210}Pb dating of recent volcanic eruptions on the sea floor, *Nature*, *368*, 841–844.

Schouten, H., M. A. Tivey, D. Fornari, D. Yoerger, A. Bradley, M. Edwards, and P. Johnson (2003), Central anomaly magnetization high: Constraints on the volcanic construction and architecture of young upper oceanic crust, EPR 9°–10°N, in *Ridge 2000 Events*, edited by D. Hassler, C. Fisher, and S. Givens, pp. 30–34, Ridge 2000 Off., University Park, Pa.

Schreiner, A. E., L. M. Dorman, and L. D. Bibee (1991), Shear wave velocity structure from interface waves at two deep water sites in the Pacific Ocean, in *Shear Waves in Marine Sediments*, edited by J. M. Hovem, R. Stoll, and M. Richardson, pp. 231–238, Kluwer Acad., Norwell, Mass.

Shearer, P. M., and J. A. Orcutt (1985), Anisotropy in the oceanic lithosphere: Theory and observations from the Ngendie seismic refraction experiment in the southwest Pacific, *Geophys. J. R. Astron. Soc.*, *80*, 493–526.

Sleep, N. H. (1991), Hydrothermal circulation, anhydrite precipitation, and thermal structure at ridge axes, *J. Geophys. Res.*, *96*, 2375–2387.

Sohn, R. A., S. C. Webb, J. A. Hildebrand, and B. D. Cornuelle (1997), Three-dimensional tomographic velocity structure of the upper crust, coaxial segment, Juan de Fuca Ridge: Implications for on-axis evolution and hydrothermal circulation, *J. Geophys. Res.*, *102*, 17,679–17,695.

Sohn, R. A., D. Fornari, K. L. Von Damm, J. A. Hildebrand, and S. C. Webb (1998), Seismic and hydrothermal evidence for a cracking event on the East Pacific Rise crest at 9°50′N, *Nature*, *396*, 159–161.

Sohn, R. A., J. A. Hildebrand, and S. C. Webb (1999), A microearthquake survey of the high-temperature vent fields on the volcanically active East Pacific Rise, *J. Geophys. Res.*, *104*, 25,367–25,378.

Stephen, R. A. (1981), Seismic anisotropy observed in upper oceanic crust, *Geophys. Res. Lett.*, *8*, 865–868.

Stephen, R. A. (1985), Seismic anisotropy in the upper oceanic crust, *J. Geophys. Res.*, *90*, 11,383–11,396.

Stevenson, J. M., and J. A. Hildebrand (1996), Gravity modeling of a volcanically active site on the East Pacific Rise axis, *Tectonophysics*, *254*, 57–68.

van Everdingen, D. A. (1995), Fracture characteristics of the sheeted dike complex, Troodos ophiolite, Cyprus: Implications for permeability of oceanic crust, *J. Geophys. Res.*, *100*, 19,957–19,972.

Von Damm, K. L. (2000), Chemistry of hydrothermal vent fluids from 9°–10°N, East Pacific Rise: "Time zero," the immediate posteruptive period, *J. Geophys. Res.*, *105*, 11,203–11,222.

Von Damm, K. L., S. E. Oosting, R. Kozlowski, L. G. Buttermore, D. C. Colodner, H. N. Edmonds, J. M. Edmond, and J. M. Grebmeier (1995), Evolution of East Pacific Rise hydrothermal vent fluids following a volcanic eruption, *Nature*, *375*, 47–50.

Wang, K., and E. E. Davis (1996), Theory for the propagation of tidally induced pore pressure variations in layered subseafloor formations, *J. Geophys. Res.*, *101*, 11,483–11,495.

White, R. S., and R. B. Whitmarsh (1984), An investigation of seismic anisotropy due to cracks in the upper oceanic crust at 45°N, Mid-Atlantic Ridge, *Geophys. J. R. Astron. Soc.*, *79*, 439–468.

Whitmarsh, R. B., and R. C. Lilwall (1982), A new method for the determination of in-situ shear-wave velocity in deep-sea sediments, paper presented at Oceanology International 1982, Spearhead Exhibitions, Kingston-upon-Thames, U. K.

Wilkens, R. H., G. J. Fryer, and J. Karsten (1991), Evolution of porosity and seismic structure of upper oceanic crust: Importance of aspect ratios, *J. Geophys. Res.*, *96*, 17,981–17,995.

J. A. Hildebrand, Scripps Institution of Oceanography, University of California, San Diego, 9500 Gilman Dr., La Jolla, CA 92093-0205, USA. (jah@mpl.ucsd.edu)

R. A. Sohn, Woods Hole Oceanographic Institution, Woods Hole, MA 02543, USA. (rsohn@whoi.edu)

S. C. Webb, Lamont-Doherty Earth Observatory, 61 Route 9W, PO Box 1000, Palisades, NY 10964-8150, USA. (scw@ldeo.columbia.edu)